NANO LETTERS

2008
Vol. 8, No. 2
624−630

# Nanoparticle-Induced Enhancement and Suppression of Photocurrent in a Silicon Photodiode

**Sri Priya Sundararajan, Nathaniel K. Grady, Nikolay Mirin, and Naomi J. Halas***

*Department of Electrical and Computer Engineering, Department of Chemistry, and the Laboratory for Nanophotonics, Rice University, 6100 Main Street, Houston, Texas 77005*

*Received November 20, 2007; Revised Manuscript Received January 3, 2008*

**ABSTRACT**

**Nanoparticles are capable of both enhancing and suppressing the photocurrent in a silicon diode when deposited on the active face of the device. Photocurrent imaging of the individual nanoparticles and nanoparticle aggregates responsible for this effect reveals that Au nanospheres, nanoshells, and nanoshell dimers each exhibit unique wavelength-dependent suppression-enhancement characteristics. In contrast, silica nanospheres provide a sizable and relatively uniform photocurrent enhancement across the same spectral range (532–980 nm). Unusual light-harvesting behavior observed correlates with a highly complex energy flow (optical "vortexing") for the forward scattered light of plasmon resonant nanoparticles into the device.**

Photoinduced carrier generation and charge separation are the requisite processes of solar cells and photodetectors. In the photosynthetic reaction center of plants, nature has merged these two functions to achieve almost unit efficiency; however, in man-made devices their integration remains a critical challenge. The combined needs for light harvesting and voltage or current generation drive device design, bringing photoabsorbers directly into the active region of the device, as in the case of photoelectrochemical cells.[1] Another approach is to implement light-harvesting strategies in a separate processing step, by adding light-absorbing molecules or by positioning or patterning light-harvesting antenna structures onto the active face of a fabricated device.[2] This latter approach may offer methods for further increasing efficiencies of devices already in use or in production. If relatively inexpensive, mass-producible nanoparticles could serve as effective light-harvesting nanoantennas, significant improvements in device efficiency and performance for photodetectors and solar cells may be obtainable at relatively low cost for widespread use.

Recent experiments have shown that Au nanoparticles can be used as light-harvesting nanoantennas when deposited at remarkably low coverage on the active face of silicon solar cells.[3−6] The nanoparticles showed a measurable, wavelength dependent increase in device efficiencies in both shallow and buried pn junction devices. The junction depth dependence suggests two regimes of nanoparticle-induced light harvesting. For deep junction devices, the forward scattered field (nominally within several particle diameters) affects photocurrent generation,[7] while for very shallow junction devices, the nanoparticle near field can enhance photocurrent generation in the active region close to the device surface.[8,9] It is highly likely that the properties of the specific individual nanoparticles, such as absorption and scattering cross section and plasmon resonances, controlled by their size and shape, play a critical role in light harvesting in these types of device structures. However, the nanoparticle-dependent aspects of this highly promising light-harvesting strategy have not yet been investigated.

Here, we report a study of the changes in photocurrent in a buried silicon photodiode induced by nanoparticles of differing properties: Au nanoparticles, Au nanoshells and nanoshell aggregates varying in size and plasmon resonance frequency, and silica nanospheres. Photocurrent imaging, initially developed to obtain charge mapping in individual nanoscale devices,[10] is used here to measure the effect of each individual nanoparticle on the electrical response of the device. Plasmonic nanoparticles can either enhance or suppress photocurrent in the device depending on wavelength, nanoparticle resonance, and nanostructure size and geometry. This surprising response is directly related to the complex energy flow of scattered light by plasmonic nanoparticles, an effect previously predicted for radiatively damped metallic nanoparticles in vacuum, but not yet experimentally observed. In contrast, dielectric scatterers provide a uniform photocurrent enhancement across a broad spectral range.

* Corresponding author. E-mail: halas@rice.edu.

10.1021/nl073030+ CCC: $40.75 
**Published on Web 01/23/2008**

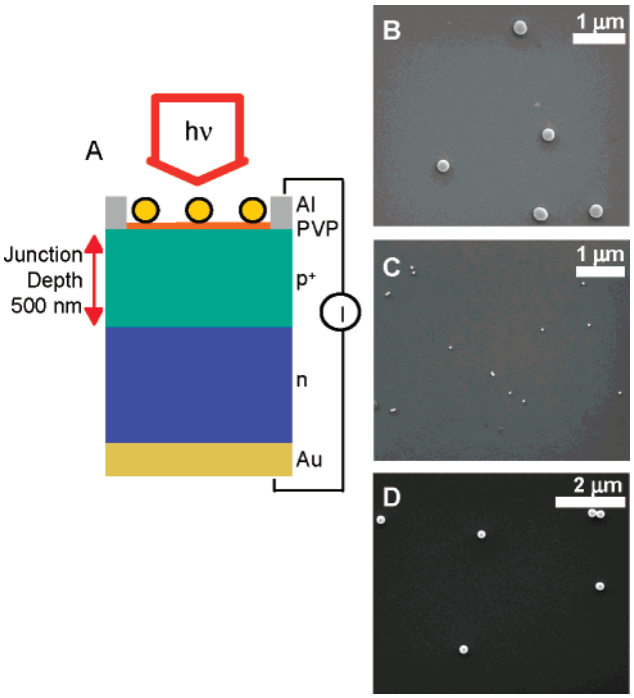


**Figure 1.** (A) Schematic of the nanoparticle functionalized $p^+n$ photodiode. Right: Scanning electron micrograph images, indicating representative densities of nanoparticle surface coverage on devices for (B) $r = 60$ nm silica particles, (C) $r = 25$ nm Au colloid, and (D) $[r_1, r_2] = [96, 116]$ nm nanoshells.

Our experimental geometry consisted of silicon photodiodes functionalized with nanoparticles on their light-collecting face (Figure 1A). Silicon $p^+n$ diodes (Addison Engineering, Inc., San Jose, CA) were fabricated on 0.010−0.020 Ω cm resistivity n-type wafers. The junction depth was 500 nm, determined by destructive profiling of one of the devices (Solecon Laboratories, Reno, NV). The surface carrier concentration within the first 200 nm of device is p-type and ranges from $4 \times 10^{19}$ to $1 \times 10^{20}$ $cm^{-3}$. The front aluminum contact thickness is a 3 mm wide × 500 nm thick edging running along all four sides of the rectangular die (2.0 cm × 2.2 cm) while the back contact is a 475 nm thick gold layer coating the entire back surface. Five types of nanoparticles were used to functionalize the active face of the photodiodes. Solid silica nanospheres ($r = 60$ nm, Precision Colloid, Cartersville, GA) and solid Au nanospheres ($r = 25$ nm, Ted Pella, Redding, CA) were obtained commercially. Three different sizes of Au−silica nanoshells with $[r_1, r_2] = [38, 62]$ nm, $[r_1, r_2] = [62, 81]$ nm, $[r_1, r_2] = [96, 116]$ nm, where $r_1$ is the inner silica core radius and $r_2$ is the total particle radius, were prepared on commercially available silica cores (Precision Colloids, Cartersville, GA and Nissan Chemical, Houston, TX) using the seeded growth technique previously reported. The $p^+n$ photodiodes were cleaned by sonication in ethanol and dried in a stream of nitrogen. The nanoparticles were deposited from aqueous suspension onto the diode faces prefunctionalized with poly(vinyl pyridine).[11] The deposition times and precursor nanoparticle suspension concentrations were selected to maintain interparticle spacings much greater than the laser spot size, yet to ensure sufficiently dense surface coverage that multiple particles could be imaged in each 15 × 15 μm area scan (Figure 1).

Maps of the local photocurrent were obtained by scanned imaging of the functionalized photodiodes using a fiber-coupled confocal sample-scanning optical microscope with 532, 633, 785, and 980 nm wavelength laser sources (α−SNOM, WITec GmbH, Ulm, Germany). A 100x/0.9 NA microscope objective provided a diffraction-limited laser spot on the surface of the photodiode. The sample is raster-scanned using a piezo stage, typically over a 15 × 15 μm area with 128 × 128 pixels at an integration time of 0.15 s/pixel for 532, 633, or 785 nm and 0.83 s/pixel for 980 nm. At each pixel, the reflected light (detected with a photomultiplier tube) and the photocurrent were obtained simultaneously using standard lock-in techniques (SR540 and SR850, Stanford Research Systems, Sunnyvale, CA) at a ∼400 Hz chopping rate. No sample biases were applied. The simultaneous collection of confocal reflectance and photocurrent permits the correlation of nanoparticle position with an increase or decrease of photocurrent at the same point. The incident laser power was monitored during the measurement with a silicon photodiode (DET110, Thor Labs, Newton, NJ). The incident laser intensity was adjusted to obtain a photocurrent of approximately 2.5 nA at wavelengths of 532, 633, and 785 nm and 0.6 nA at 980 nm.

To obtain the local enhancement at each nanostructure, the scan line containing the strongest photocurrent due to the particle ($I_{particle}$) was obtained, then compared to the average local background level ($I_{background}$) along this linear scan. The change in photocurrent due to the presence of the nanoparticle is

$$\frac{\Delta I}{I} \equiv \frac{I_{particle} - I_{background}}{I_{background}} \quad (1)$$

This local determination of photocurrent enhancement due to each individual nanoparticle is advantageous because individual nanoparticle contributions can be clearly distinguished from enhancements due to variations in nanoparticle surface coverage density. In addition, this approach removes any effect of long-term laser power drift or large-range (micron or millimeter scale) spatial inhomogeneities in the response of the device structure. In our photocurrent images the nanoparticle appears bright if its presence increases the measured photocurrent and dark if its presence suppresses the photocurrent at that location. The apparent size of the nanostructure-associated feature in the photocurrent images is a convolution of the laser spot size and the nanostructure influenced portion of the substrate. Because this measurement does not specifically resolve the topology of the nanostructure, this approach can be combined with atomic force microscopy to obtain the specific nanostructure geometry responsible for each local change in photocurrent.

Photocurrent images for all types of nanoparticles studied at the four wavelengths used in the experiment were obtained (Figure 2). The images in the top row correspond to silica nanospheres of 60 nm radius, (A−D), in the second row Au nanoparticles of 25 nm radius (E−F), followed by (third row)

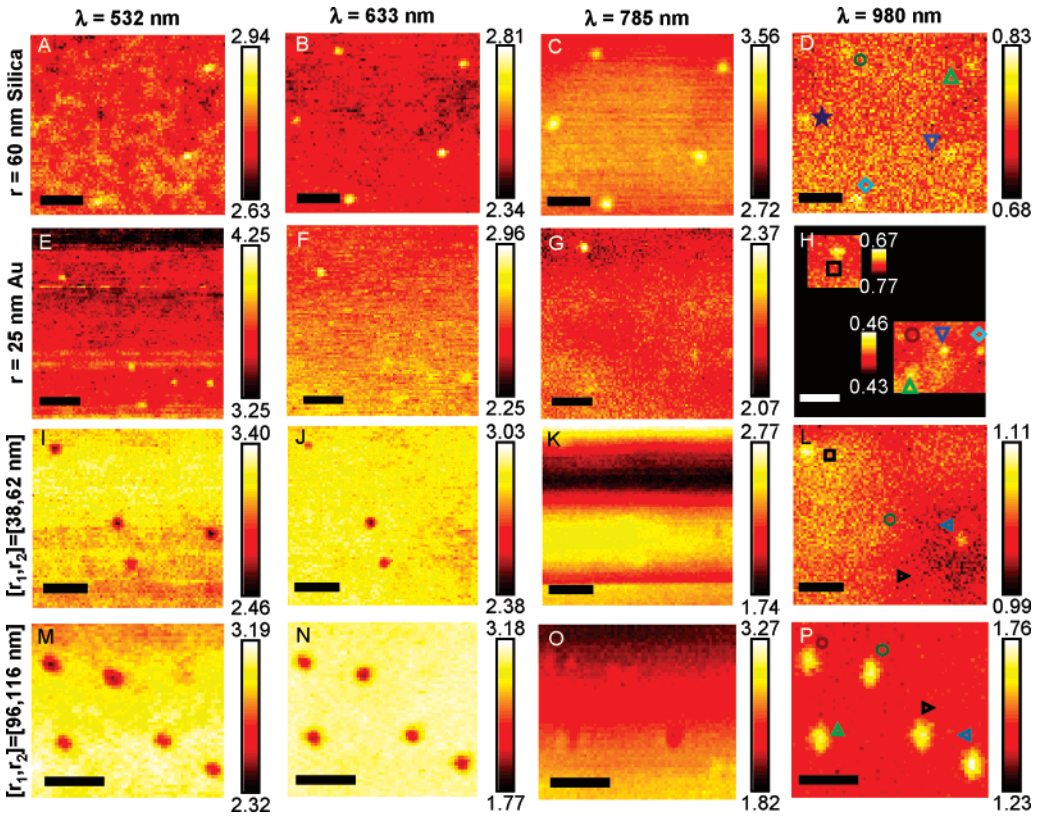


**Figure 2.** Photocurrent images [in nanoamperes] of (A−D) $r = 60$ nm silica nanospheres, (E−H) $r = 25$ nm solid Au nanospheres, (I−L) $[r_1, r_2] = [38, 62]$ nm nanoshells, and (M−P) $[r_1, r_2] = [96, 116]$ nm nanoshells for light incident at wavelengths of 532, 633, 785, and 980 nm. Symbols represent single nanoparticles, dimers, and higher order aggregates sampled during each scan. Scale bars are 2 $\mu$m.

Au nanoshells of dimension $[r_1, r_2] = [38, 62]$ nm (I−L), and (fourth row) Au nanoshells of dimension $[r_1, r_2] = [96, 116]$ nm. In each row, images of the same sample were obtained at the excitation wavelengths of 532, 633, 785, and 980 nm, respectively. In the four rightmost images obtained at 980 nm wavelength, individual nanoparticle features are denoted with specific symbols. The values of the changes in photocurrent $\Delta I/I$ for the individual nanoparticles of each type, corresponding to the symbols in these four images, are plotted as percentage changes in Figure 3.

These images reveal strong, nanoparticle-dependent differences in photocurrent modification due to the properties of the various types of nanoparticles studied. (Small variations in $\Delta I/I$ for the individual nanoparticles sampled may also arise from differences in the local environment of each nanoparticle due to variations in dopant or surface trap state density in the underlying device and nonuniformity in the PVP spacer layer.) Dielectric silica nanospheres (Figure 2A−D) exhibit a consistent and uniform enhancement over the entire wavelength region studied. This uniform enhancement is attributed to the very similar, nonresonant scattering properties of these particles across the measurement wavelength range. The particle-to-particle variation in enhancement is also relatively small, indicating that the nanoparticles themselves are relatively uniform in size, and well dispersed on the device with minimal or no aggregation. Au nanospheres also display a photocurrent enhancement over this wavelength range, appearing strongest at the shortest wavelength (11%) and decreasing with increasing wavelength, to

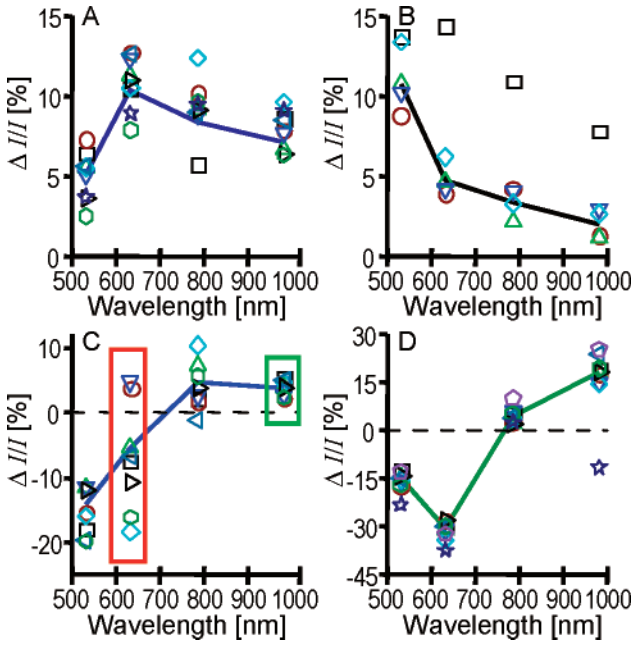


**Figure 3.** Local photocurrent modification for photodiodes functionalized with (A) $r = 60$ nm silica nanospheres, (B) $r = 25$ nm solid Au nanospheres, (C) $[r_1, r_2] = [38, 62]$ nm nanoshells, or (D) $[r_1, r_2] = [96, 116]$ nm nanoshells. Symbols correspond to particles marked in the rightmost column images of Figure 2 (Figure 2, panels D, H, L, and P, respectively). Solid lines indicate the trend of the average value. In panel C, the red square pertains to parameters modeled in Figure 4A, and the green square corresponds to Figure 4B.

3% at 980 nm. This observed wavelength dependence is generally consistent with previously reported results that did not distinguish individual nanoparticle contributions, but also shows some variation with those results.[6] For example, one of the observed Au nanoparticles in this image (denoted □) shows a wavelength-dependent enhancement that deviates significantly from the other nanoparticles in the image, revealing a significantly stronger photocurrent enhancement over the entire wavelength range. This possibly may be due to the presence of a nanoparticle aggregate at that site. Small Au nanoparticle aggregates such as dimers and trimers possess a different spectrum of plasmon resonances and a larger scattering cross section due to their larger spatial extent than their individual Au nanoparticle constituents.[12,13] The presence of even a small percentage of such aggregates, quite possible in the preparation of these types of nanoparticle-dispersed surfaces, may be responsible for additional photocurrent enhancements for this device geometry.

Au nanoshells (Figures 2I−P and 4A−D) exhibit a markedly different wavelength-dependent photocurrent enhancement-suppression characteristic than either silica or Au nanospheres. Two different sizes of nanoshells were investigated: Figure 2I−L shows the photocurrent images of $[r_1, r_2] = [38, 62]$ nm nanoshells, and Figure 2M−P shows the $[r_1, r_2] = [96, 116]$ nm nanoshell photocurrent maps. With increased total particle size, the proportion of scattering to absorption in the total extinction cross section will increase, and multipolar plasmon modes will contribute more significantly to the overall nanoshell plasmon response.[14−17] The dipolar plasmon resonances for the $[r_1, r_2] = [38, 62]$ nm and $[r_1, r_2] = [96, 116]$ nm nanoshells suspended in $H_2O$ occur at 650 and 960 nm, respectively, and a quadrupolar resonance at 697 nm is also present for the $[r_1, r_2] = [96, 116]$ nm nanoshells (see Supporting Information for spectral data for all nanoparticles). On a highly refractive substrate such as the silicon device studied here, the resonance frequencies of plasmonic nanoparticles are expected to redshift and higher order multipole plasmon modes should be preferentially enhanced.[18−23]

Both the small and large nanoshells suppress the photocurrent at wavelengths of 532 and 633 nm and enhance the photocurrent at wavelengths of 785 and 980 nm (Figures 3C,D and 4F), where the larger nanoshells show the larger photocurrent suppression and enhancement. The strongest photocurrent suppression (30%) is due to the $[r_1, r_2] = [96, 116]$ nm nanoshells at a wavelength of 633 nm (Figures 2N and 3D). The maximum photocurrent enhancement observed in these experiments, nominally 20%, was observed at 980 nm excitation for these larger nanoshells. In this case, the forward scattering of light into the device is enabled both by the strongly scattering character of the nanoshell dipolar resonance for a nanoparticle in this size range[14] and by the greater transmissivity of the 980 nm wavelength light in silicon. These large observed enhancements have important technological implications for long-wavelength sensitization of silicon photodetectors into the near IR for imaging applications, as well as for expanding the spectral response of silicon-based solar cells in that wavelength region as well. However, long wavelength photocurrent enhancement comes at the cost of shorter wavelength photocurrent suppression, a property that may impact device or nanoparticle design or applications.

By combining photocurrent imaging with atomic force microscopy, the specific nanoparticle geometry associated with each enhancement-suppression feature in the photocurrent images can be determined. This approach allows us to discriminate between the photocurrent modification due to isolated nanoshells and nanoshell aggregates also deposited on the active surface of the device. An AFM tip mounted below a standard 50× long working distance microscope objective and positioned using a high-precision piezo stage in our microscope permits the acquisition of AFM images and photocurrent images of the same area of the sample with systematic offsets of at most a few microns. This combined photocurrent-AFM measurement is seen in the case of intermediate sized $[r_1, r_2] = [62,81]$ nm nanoshells on Si photodiodes (Figure 4). A clear visible correlation between the individual nanoshells and nanoshell aggregates observed in the AFM topographic image in Figure 4E and the photocurrent images of Figure 4A−D is easily observable. In Figure 4E, the presence of both individual isolated nanoshells and nanoshell dimers and occasionally larger aggregates can be seen. From these data, we can clearly distinguish between the photocurrent suppression-enhancement characteristics of individual nanoshells and nanoshell aggregates. In contrast to the photocurrent suppression-enhancement characteristic of individual nanoshells, most of the nanoshell dimers suppress the photocurrent at all four wavelengths (Figure 4G). This is also in contrast to the nanoparticle aggregate case observed in Figure 3B, which results in photocurrent enhancement. The magnitude of the photocurrent suppression in the case of nanoshell aggregates is likely to be related to the large scattering cross section of the aggregates and may also be influenced by nanoshell dimer properties such as interparticle distance, including the cases of touching or fused dimers[13,24,25] and relative orientation of the dimer axis with respect to the polarization of the incident light. This type of broadband photocurrent suppression would no doubt be deleterious to device performance; for this device geometry nanoshell aggregates should clearly be avoided.

In general, the nanoparticle-induced photocurrent changes that are observed are related to the interference between the light scattered from the nanoparticle into the device and the light transmitted directly into the input face of the device.[6] The relative phase of these two input waves results in constructive or destructive interference, which may affect photocurrent generation if a constructive or destructive node occurs in the active region of the device. For plasmon resonant nanoparticles in particular, the behavior of the forward scattered wave can be quite complex.[26−28] Previous theoretical studies of plasmon resonant nanoparticles in vacuum have shown that the forward scattered field for frequencies on or near the plasmon resonance of the nanoparticle may have vortexlike characteristics and a spatial structure that depends quite sensitively on the properties of

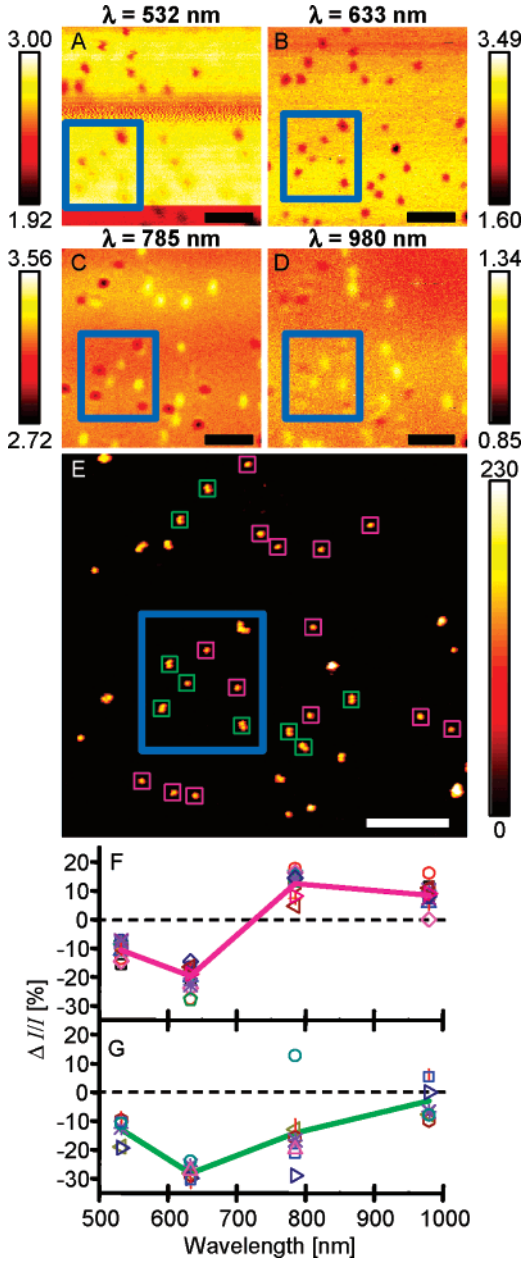


**Figure 4.** Photocurrent images [in nanoamperes] of (A−D) [$r_1$, $r_2$] = [62, 81] nm nanoshells for light incident at wavelengths of 532, 633, 785, and 980 nm. (E) Topographic (AFM) image of the same area shown in panels A−D, revealing individual nanoparticle geometry. Scale bars all correspond to 3 $\mu$m. Individual nanoshells are highlighted in magenta, nanoshell dimers in green. In panels A−E, the blue inset boxes mark a representative subset of nanoparticles replicated in each image but with varying influence on the photocurrent. (F) Photocurrent modification for isolated nanoshells and (G) dimers of nanoshells. Solid lines represent average trend. Each symbol in panels F and G corresponds to one of the marked particles in panel E.

the nanoparticle. It seems quite plausible that this vortexlike behavior may also be present for the case of a nanoparticle in vacuum with forward scattering into a Si medium and more generally may be a important property of plasmonic nanoparticle-induced light scattering into larger devices and materials.

To further examine the unusual enhancement-suppression characteristic of nanoshells in this basic device geometry, finite element simulations were performed for [$r_1$, $r_2$] = [38, 61] nm nanoshells on a silicon slab using the commercially available COMSOL modeling package. The incident light was modeled as a plane wave linearly polarized in the *x*-direction, propagating into the device (*z*-direction). Mirror boundary conditions were applied at lateral faces of the simulation domain. These boundary conditions were chosen to best approximate the sparse surface coverage regime studied experimentally where adjacent nanoparticles are spaced by several particle diameters and interparticle interactions are minimal. The period of the square array of nanoparticles thus simulated is set by the *x* and *y* extent of the simulation domain. In a regime where the domain extent was not sufficiently large, interparticle interactions were manifest as spots of intense electric field near the domain boundaries. In the case of a [$r_1$, $r_2$] = [38, 61] nm nanoshell, a simulation domain size of 800 nm in both *x*- and *y*-directions was used. This extent was found to be sufficiently large to avoid interparticle interaction effects due to strong scattering of light by the nanoshell. The extent of the slab in the *z*-direction was 1.5 $\mu$m. A scattering boundary condition was applied at the exit face, and a perfectly matched layer absorbing in the *z*-direction was implemented adjacent to it to eliminate extraneous reflections. The dielectric functions for Au and Si were obtained from Johnson and Christy[29] and Adachi,[30] respectively.

The parameters used in this simulation correspond to experimental parameters that showed unusual and contrasting behavior. In our experimental data, the 633 nm photocurrent images for [$r_1$, $r_2$] = [38, 61] nm nanoshells showed an anomalously wide variation in modified photocurrent, varying from +5 to −20% (Figure 3C, red). In contrast, the photocurrent measurements for the same nanoparticles on the same sample at 980 were quite consistent and well behaved (Figure 3C, green), indicating that the large variation observed in the 633 nm data was not due to inhomogeneities in the nanoparticles or the device. In Figure 5, the Poynting vector field through the Si slab is overlaid onto the electric field magnitude in the *yz* plane for the case of an [$r_1$, $r_2$] = [38, 61] nm Au nanoshell is shown for 633 and 980 nm wavelength incident plane waves. At 633 nm (Figure 5a), the presence of the nanoshell clearly disrupts the power flow well into the Si slab. Vortexlike behavior[26,31] of the forward scattered field is clearly observed in this simulation, throughout the depth of the Si slab used to model the device. At this incident wavelength, the average energy flow across this plane is directed toward the surface and toward the nanoparticle with the energy concentrated near the nanoparticle−silicon interface. In contrast, at the incident field wavelength of 980 nm (Figure 5b) the scattered light into the device is well behaved with energy flow directed toward the bottom surface of the device and with a uniform distribution of energy throughout the entire simulation region. This type of behavior may need to be an important consideration in devices where plasmonic nanoparticles are used in light collection or transmission and also may be relevant to the properties of other types of nanoantennas, such as nanofab-

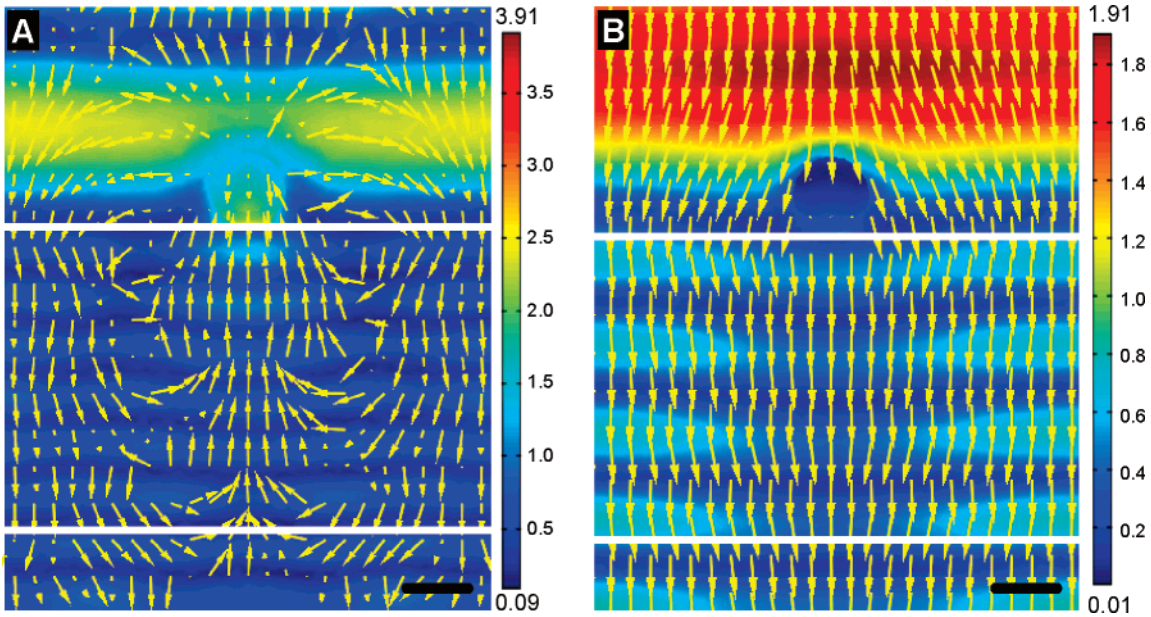


**Figure 5.** Poynting vector field plots show power flow through a $[r_1, r_2] = [38, 61]$ nm nanoshell on a Si slab at (A) 633 nm and (B) 980 nm, corresponding to the data points shown in Figure 3C enclosed in red and green, respectively. Arrows are normalized for power flow magnitude and indicate direction of power flow. The top and bottom white lines indicate the air−Si interface at $z = 0$ and at a depth of 500 nm, respectively. These cross sections are in the *yz* plane, perpendicular to the incident light polarization. The Poynting vector field is overlaid onto the norm of the vector electric field (indicated by colorbar).

ricated bowtie structures, implemented on device structures for the same light-harvesting function.

In conclusion, we have investigated nanoparticle-induced photocurrent enhancement and suppression in a silicon photodiode, focusing on the influence of the nanoparticle properties on this effect. Imaging the changes in photocurrent due to individual nanoparticles positioned on the active face of the device has allowed us to investigate the effect of specific nanoparticle type, which will be directly relevant to enhancing device efficiencies. Several important conclusions are obtained from this study. While plasmonic nanoparticles have been of interest for photocurrent enhancement in these types of device structures, this study also indicates that nonresonant dielectric nanoparticles provide photocurrent enhancement over a wide wavelength range. Therefore silica nanoparticles should be considered promising candidates for boosting light-harvesting efficiencies at low cost in certain types of devices. Plasmonic nanoparticles have quite widely varying enhancement-suppression characteristics, depending on nanoparticle size, geometry, and plasmon resonance wavelength, which may lend themselves most favorably to specific applications such as sensitizing the response of photodetectors over specific wavelength regions. However, where individual nanoparticles may provide photocurrent enhancement at certain wavelengths, aggregates of the same nanoparticle may in fact suppress photocurrent at those same wavelengths and degrade device performance, an important fabrication and manufacturing consideration. Finally, for certain cases the energy flow associated with the forward scattered field of a plasmonic nanoparticle exhibits a complex spatial structure. This vortexlike behavior may very well influence photocurrent enhancement at the wavelengths where it occurs. While this property had been previously studied theoretically for the case of a metallic nanoparticle in vacuum, our observations may indicate that this interesting behavior may be quite important in the design and development of nanoparticle-enhanced light-collecting devices such as infrared detectors and solar cells.

**Acknowledgment.** The authors would like to thank Jason Deibel and Yaroslav Urzhumov for helpful discussions regarding the COMSOL finite element modeling package. The authors would like to thank Oara Neumann, Carly Levin, and Nche Fofang for their assistance in preparation of nanoshells for these studies. We gratefully acknowledge support for this work from United Technologies Corp./Air Force Office of Scientific Research under Grant 05-S531-035-C1, the Texas Institute for Bio-Nano Materials and Structures for Aerospace Vehicles funded by the NASA URETI program, and the Robert A. Welch Foundation under Grant C-1220.

**Supporting Information Available:** The extinction spectra for the aqueous nanoparticle suspensions used in this study are included in the supplemental information section. This material is available free of charge via the Internet at http://pubs.acs.org.

## References

(1) Oregan, B.; Gratzel, M. *Nature* **1991**, *353*, 737−740.
(2) Catchpole, K. R. *Philos. Trans. R. Soc. London, Ser. A* **2006**, *364*, 3493−3503.
(3) Schaadt, D. M.; Feng, B.; Yu, E. T. *Appl. Phys. Lett.* **2005**, *86*, 63106.
(4) Derkacs, D.; Lim, S. H.; Matheu, P.; Mar, W.; Yu, E. T. *Appl. Phys. Lett.* **2006**, *89*, 93103.
(5) Pillai, S.; Catchpole, K. R.; Trupke, T.; Green, M. A. *J. Appl. Phys.* **2007**, *101*, 093105.
(6) Lim, S. H.; Mar, W.; Matheu, P.; Derkacs, D.; Yu, E. T. *J. Appl. Phys.* **2007**, 101.
(7) Stuart, H. R.; Hall, D. G. *Appl. Phys. Lett.* **1996**, *69*, 2327−2329.
(8) Ohashi, K.; Baba, T.; Makita, K.; Fujikata, J.; Ishi, T. *Jpn. J. Appl. Phys.* **2005**, *44*, L364−L366.

(9) Hesselink, L.; Saraswat, K. C.; Yuen, Y.; Matteo, J. A.; Okyay, A. K.; Miller, D.; Tang, L. *Opt. Lett.* **2006**, *31*, 1519−1521.
(10) Balasubramanian, K.; Burghard, M.; Kern, K.; Scolari, M.; Mews, A. *Nano Lett.* **2005**, *5*, 507−510.
(11) Chumanov, G.; Luzinov, I.; Malynych, S. *J. Phys. Chem. B* **2002**, *106*, 1280−1285.
(12) Nordlander, P.; Oubre, C.; Prodan, E.; Li, K.; Stockman, M. I. *Nano Lett.* **2004**, *4*, 899−903.
(13) Romero, I.; Aizpurua, J.; Bryant, G. W.; Garcia De Abajo, F. J. *Opt. Express* **2006**, *14*, 9988−9999.
(14) Oldenburg, S. J.; Hale, G. D.; Jackson, J. B.; Halas, N. J. *Appl. Phys. Lett.* **1999**, *75*, 1063−1065.
(15) Lin, A. W. H.; Lewinski, N. A.; West, J. L.; Drezek, R. A.; Halas, N. J. *J. Biomed. Opt.* **2005**, *10*, 64035.
(16) Grady, N. K.; Nordlander, P.; Halas, N. J. *Chem. Phys. Lett.* **2004**, *399*, 167−171.
(17) Tam, F.; Chen, A. L.; Kundu, J.; Wang, H.; Halas, N. J. *J. Chem. Phys.* **2007**, *127*, 204703.
(18) Tam, F.; Moran, C.; Halas, N. J. *J. Phys. Chem. B* **2004**, *108*, 17290−17294.
(19) Nordlander, P.; Prodan, E. *Nano Lett.* **2004**, *4*, 2209−2213.
(20) Saiz, J. M.; Gonzalez, F.; Moreno, F. *Opt. Lett.* **2006**, *31*, 1902−1904.
(21) Grechko, L. G.; Gozhenko, V. V.; Whites, K. W. *Phys. Rev. B* **2003**, *68*, 125422.
(22) Prodan, E.; Lee, A.; Nordlander, P. *Chem. Phys. Lett.* **2002**, *360*, 325−332.
(23) Prodan, E.; Nordlander, P.; Halas, N. J. *Chem. Phys. Lett.* **2003**, *368*, 94−101.
(24) Brandl, D. W.; Oubre, C.; Nordlander, P. J. *J. Chem. Phys.* **2005**, *123*, 024701.
(25) Oubre, C.; Nordlander, P. *J. Phys. Chem. B* **2005**, *109*, 10042−10051.
(26) Zheludev, N. I.; Fedotov, V. A.; Bashevoy, M. V. *Opt. Express* **2005**, *13*, 8372−8378.
(27) Tribelsky, M. I.; Luk'yanchyk, B. S. *Phys. Rev. Lett.* **2006**, *97*, 263902.
(28) Luk'yanchyk, B. S.; Tribelsky, M. I.; Wang, Z. B.; Hong, M. H.; Shi, L. P.; Chong, T. C. *Appl. Phys. A* **2007**, *89*, 259−264.
(29) Johnson, P. B.; Christy, R. W. *Phys. Rev. B* **1972**, *6*, 4370−4379.
(30) Adachi, S. *Optical Constants of Crystalline and Amorphous Semiconductors*; Kluwer Academic Publishers: Norwell, MA, 1999.
(31) Chong, T. C.; Lin, Y.; Hong, M. H.; Luk'yanchuk, B. S.; Wang, Z. B. *Phys. Rev. B* **2004**, *70*, 035418.

NL073030+